This is a repository copy of *Shear stress rosettes capture the complex flow physics in diseased arteries*.

White Rose Research Online URL for this paper:
https://eprints.whiterose.ac.uk/157805/

Version: Accepted Version

Article:
Krishna, C.V., Suja, V.C., Watton, P. orcid.org/0000-0002-5531-5953 et al. (2 more authors) (2020) Shear stress rosettes capture the complex flow physics in diseased arteries. Journal of Biomechanics, 104. 109721. ISSN 0021-9290

https://doi.org/10.1016/j.jbiomech.2020.109721

Article available under the terms of the CC-BY-NC-ND licence (https://creativecommons.org/licenses/by-nc-nd/4.0/).

Reuse
This article is distributed under the terms of the Creative Commons Attribution-NonCommercial-NoDerivs (CC BY-NC-ND) licence. This licence only allows you to download this work and share it with others as long as you credit the authors, but you can't change the article in any way or use it commercially. More information and the full terms of the licence here: https://creativecommons.org/licenses/

Takedown
If you consider content in White Rose Research Online to be in breach of UK law, please notify us by emailing eprints@whiterose.ac.uk including the URL of the record and the reason for the withdrawal request.

eprints@whiterose.ac.uk
https://eprints.whiterose.ac.uk/

Shear Stress Rosettes Capture the Complex Flow Physics in Diseased Arteries

C. Vamsi Krishna[1,a+], Vineeth Chandran Suja[1,b], Paul N Watton[c,d], Jaywant H Arakeri[a], and Namrata Gundiah[a*]

[a]Department of Mechanical Engineering, Indian Institute of Science, Bangalore, India 560012

[b]Department of Chemical Engineering, Stanford University, Stanford, California 94305-5025

[c]Department of Computer Science & INSIGNEO Institute for In Silico Medicine, University of Sheffield, Sheffield, UK.

[d]Department of Mechanical Engineering and Materials Science, University of Pittsburgh, Pittsburgh, US

* For correspondence:

Namrata Gundiah

Department of Mechanical Engineering, Indian Institute of Science, Bangalore 560012.

Email: namrata@iisc.ac.in, ngundiah@gmail.com **Tel (Off/ Lab)**: 91 80 2293 2860/ 3366

[1] These authors contributed equally

+ Present address:

Department of Aerospace and Mechanical Engineering, University of Southern California – Los Angeles, California - 90089

Resubmitted to Journal of Biomechanics 3 January, 2020

Abstract

Wall shear stress (WSS) is an important parameter in arterial mechanobiology. Various flow metrics, such as time averaged WSS (TAWSS), oscillatory shear index (OSI), and transWSS, have been used to characterize and relate possible WSS variations in arterial diseases like aneurysms and atherosclerosis. We use a graphical representation of WSS using shear rosettes to map temporal changes in the flow dynamics during a cardiac cycle at any spatial location on the vessel surface. The presence of secondary flows and flow reversals can be interpreted directly from the shape of the shear rosette. The mean WSS is given by the rosette centroid, the OSI by the splay around the rosette origin, and the transWSS by its width. We define a new metric, anisotropy ratio (AR), as the ratio of the length to width of the shear rosette to capture flow bi-directionality. We characterized the flow physics in controls and patient specific geometries of the ascending aorta (AA) and internal carotid artery (ICA) which have fundamentally different flow dynamics due to differences in the Reynolds and Womersley numbers. The differences in the flow dynamics are well reflected in the shapes of the WSS rosettes and the corresponding flow metrics.

KEYWORDS: arterial flows, secondary flows and bidirectionality, shear metrics, aneurysms

1. Introduction

Arterial curvature, coupled with flow pulsatility (Berger *et al* 1996), results in formation of a rich variety of vortical structures (Sudo *et al* 1992; Timité, Castelain and Peerhossaini 2010; Jarrahi *et al* 2011; Glenn *et al* 2012; Bulusu and Plesniak 2013), flow reversals (Chandran and Yearwood 1981; Yearwood and Chandran 1982; Talbot and Gong 1983; Komai and Tanishita 1997), flow separations (Talbot and Gong 1983; Hamakiotes and Berger 1988), and WSS stagnation/ fixed points (Arzani *et al* 2016; Arzani and Shadden 2018). Hemodynamics plays a fundamental role in the initiation, growth, and rupture of atherosclerotic plaques and aneurysms (Ku 1997; Chatzizisis *et al* 2007; Chien 2007; Chiu and Chien 2011; Chen *et al* 2013; Robertson and Watton 2013; Baeyens and Schwartz 2016; Baeyens *et al* 2016). Wall shear stress (WSS), imposed on the endothelial cell (EC) layer lining the arterial lumen, is a critical factor in maintaining vascular homeostasis *via* the transduction of mechanical signals into specific biochemical pathways (Caro *et al* 1971; Zarins *et al* 1983; Asakura and Karino 1990; Malek *et al* 1999). Regions of low WSS creates complex hemodynamics that induces the creation of oxygen free radicals in addition to apoptosis and migration of the vascular smooth muscle cells in the arterial wall (Penn *et al* 2011). Elevated WSS and high positive spatial WSS gradient are both implicated in the initiation and rupture of aneurysms (Kulcsár *et al* 2011).

Various shear metrics have been used to characterize possible links between hemodynamic stimuli and vessel dysfunction. Oscillatory Shear Index (OSI), Aneurysm Formation Indicator (AFI), Time Averaged Wall Shear Stress (TAWSS), Relative Residence Time (RRT), and gradients in the WSS are some of the many indices, primarily defined based on unidirectional flows, which are used to describe aneurysm growth rates (Mantha *et al* 2006). A few metrics, such as Directional Oscillatory Shear Index (DOSI) and transWSS, are based on bi-directional WSS (Chakraborty *et al* 2012; Peiffer *et al* 2013; Peiffer *et al* 2013;

Wang *et al* 2013; Morbiducci *et al* 2015). Each of the different shear metrics describe different features of the complex changes in WSS. Polar plots or shear rosettes, showing variations in the WSS at a given spatial location as a function of time, provide a more complete and useful representation of the flow physics as compared to shear metrics alone. Suo and colleagues were among the early researchers to present polar plots to explore the differences in the magnitude and direction of the WSS in atherogenesis (Suo *et al*, 2007). Their data showed the importance of changes in the WSS magnitude or direction which correspond with higher expression of atherogenic proteins. More recent studies in orbital shakers use shear rosettes to quantify the role of shear stress in the radial and tangential directions in endothelial cell morphology (Potter *et al*, 2011; Weinberg *et al*, 2017; Weinberg *et al*, 2018). However, there has been little discussion and interpretation of the rosettes and their relationship to the different shear metrics and to physics of arterial flows.

In this study, we show how the shape and size of the shear rosette is a complementary method that provides useful information on the complete details regarding the WSS variations environment over a cardiac cycle. The rosette is not a substitute for any proposed metrics in the literature but may be used to infer. We graphically relate the shear rosette to the directions and values of the TAWSS variations, mean WSS, OSI and transWSS metrics at a point in the flow during a cardiac cycle. We compute flows in two different geometries of arteries corresponding to a large artery, the ascending aorta and a small artery, the internal carotid artery (ICA). Flows in these vessels are different as they have significantly different Reynolds numbers (Re) and Womersley number (α). We define the anisotropy ratio metric (AR), intimately linked to the secondary flows, as an alternate method to capture the bidirectionality in WSS and can be easily inferred from the shapes of the shear rosettes by taking the ratio of the length to width of the rosette. Changes in the endothelial morphologies under steady, oscillating, and disturbed flow conditions are causally linked to differential

inflammatory and atherogenic gene expression levels that lead to atherosclerotic plaque formation (Chiu and Chien, 2011). The shear rosette may be used in studies to infer the signaling pathways involved in the mechanosensing effects of shear stress magnitude, flow frequency, and flow direction that contribute to athero-susceptibility (Baeyens and Schwartz, 2016). An understanding of the local flow conditions in arteries is a first step to exploring the effects of mechanical factors on EC signalling that have the potential to aid in the diagnosis and treatment options in cardiovascular disease ~~(Chiu and Chien, 2011)~~.

2. Methods

2.1 Computational Fluid Dynamics (CFD) simulations in patient specific models of AA and ICA

We include patient specific geometries of an aortic aneurysm (AA) and ICA and the corresponding control geometries for both these vessels. CT data from a 54 year old male patient undergoing thoracic aortic repair *via* a Bentall procedure at the Narayana Health hospital in Bangalore, India was used to construct the geometry of AA based on methods described in Appendix A (Figure 1b). Informed consent was obtained based on established IRB approved protocols at the Institute and hospital. Control AA geometry, consisted of a 180^{o} curved circular pipe of diameter 32 mm and curvature ratio, β (a/R) = 0.38 (Figure 1a). We reconstructed a realistic model of ICA, sans sub-branches, using an open-source aneurisk database (patient id: C0088b) to have a constant diameter from the centreline coordinates of the artery (Aneurisk-Team, 2012). The control ICA geometry had a length of 72 mm from the inlet, and curvatures in multiple planes such that the maximum curvature ratio ~ 0.7 (Figure 1c). We also used the geometry of an ICA from a patient with sidewall intracranial aneurysm (Figure1d) from the European @neurIST database (Villa-Uriol *et al* 2011, Chen *et al* 2013). Typical Re, α, Dean's numbers and β in the AA are ~3000, 34, ~1900 and ~0.38 whereas these are ~450, 3, ~400 and range from 0.3-0.7 for the ICA.

Reconstructed geometries were imported into ANSYS® ICEM CFD 13.0 (ANSYS Inc., Canonsburg, Pennsylvania) and unstructured meshes were created (Appendix A). Walls were assumed to be rigid, and the fluid was modelled to be Newtonian with constant density ($\rho = 1055\ kg/m^3$) and dynamic viscosity ($\mu = 0.0049\ Ns/m^2$). We used mass flow boundary condition at the inlet and constant pressure boundary condition at the outlet. The volume flow rate in the AA geometries was specified (Figure 2a) corresponding to physiological flow rates (Olufsen *et al* 2000). Regions marked blue correspond to the acceleration, red the deceleration, and black, the dwell phase. Similarly, a physiological volume flow rate corresponding to the ICA was specified at the inlets for the geometry (Figure 1c) and are shown in Figure 2b. The dwell phase is clearly absent in the ICA case as compared to AA which has dwell phase of 0.7s. The volume flow rate (inlet) and pressure (outlet) waveforms used with the ICA were extracted from a 1D model of the artery from the @neufuse software (Reymond *et al* 2009). The governing Navier-Stokes equations along with the boundary conditions were solved using a commercial finite-volume based solver (ANSYS® FLUENT 13.0). A time step of 10^{-3} s was used for all geometries and the criterion for convergence for residuals was set below 10^{-5} for each of the continuity and the three velocity components in each case. Grid independence studies were carried out based on the following criterion: the RMS difference of WSS between successive meshes was less than 2% of the RMS of the WSS over one cardiac cycle. The number of cells were doubled until this criterion was met. Flow cycle independence was also checked until the shear rosettes were time periodic to eliminate the initial transient effects (details in Appendix A). Four cardiac cycles were simulated and results corresponding to the last cycle are reported in this study. Grid and flow cycle independence were achieved for the control aorta, ICA control, and ICA aneurysm. The number of elements for each geometry are included in Appendix A.

3. Results and Discussion

There are two main contributions of this study. First, we map the fluid dynamics in AA and ICA geometries where flows are very different. Pulsatility is higher in AA whereas flow in smaller vessels, like ICA, are less pulsatile (Berger *et al* 1996). We show that the different flows features are better represented using shear rosettes. Rosette size gives a measure of the magnitude of WSS whereas its shape represents the bi-directionality extent. Second, we show that the shear rosette allows us to obtain a graphical understanding of the different hemodynamic metrics. Table I lists definitions of relevant metrics with brief descriptions.

3.1 Shear rosettes present a pictorial representation of the WSS

Figure 3 shows numerical simulations for control AA geometry that were done using ~~.~~ ~~We used~~ a toroidal coordinate system ~~where ψ direction is in the stream-wise direction and ϕ is in the azimuth (Appendix A)~~. Axial velocity contours with superimposed velocity vectors are shown on three transverse planes (P45, P90 & P135) and the medial plane for time points corresponding to peak velocity (Figure 3a) and at the end of systole (Figure 3b). Strong secondary flows along the walls, continually changing in time, and caused by an imbalance between the radial pressure gradient and centrifugal forces, are observed in the AA (Krishna *et al,* 2017). During the diastolic phase, flow separations occur on the inner wall which are clearly seen in the transverse plane (Figure 3b). Such separations are typical of large arteries with curvatures (Chandran and Yearwood, 1981; Hamakiotes and Berger, 1988).

Figure 4 shows the shear rosettes at select points on the plane marked P135 corresponding to flow in the control AA geometry at the 135° plane. These points are individual grid elements in the geometry. WSS in a straight pipe with unsteady flow is aligned along the axial direction. Because of the presence of secondary flows and separations,

the shear stress in curved pipes need not be oriented along the axial direction. We choose two local reference directions $\hat{s}$ and $\hat{b}$ to characterize the shear rosettes at a given point on the wall. $\hat{s}$ was defined as the WSS direction at the first time step of the first cardiac cycle from the numerical simulations. $\hat{b}$ was perpendicular to $\hat{s}$ and is the local surface normal. Secondary flows are absent at the start of the first cardiac cycle. Thus $\hat{s}$ gives the direction of flow before viscous effects manifest themselves. Other reference directions, such as the direction of the average WSS, may also be chosen which would only change the orientation of the rosette.

The WSS vector changes magnitude and direction through the cardiac cycle. Component of the WSS vector in the axial direction (τ_s), marked 0°, is due to the axial flow whereas the component of the WSS vector along $\hat{b}$ (τ_b) is due to the secondary flows. In a shear rosette, we plot the magnitude and direction of the WSS at each instant of the cardiac cycle. Arrows in the rosette at location ~~H~~ B (Figure 1a) are at equally spaced time intervals (Figure 4a). Rosette segments are color-coded for the different phases in the physiological profile (Figure 2). Circles about the origin in the rosette plot indicate constant WSS magnitudes. The principal directions are labelled '1' and '2'; τ_1 and τ_2 refer to the WSS components in the principal directions (Appendix B).

3.2 Relationship between rosette and the various shear metrics for the AA geometry

The secondary flow velocities in the AA are small during the initial phase of the cardiac cycle (Krishna *et al,* 2017) and the WSS vectors at all spatial locations are hence oriented in the axial direction, θ=0°. The angular position, indicated by θ, is the polar coordinate in the shear rosette marked in the anticlockwise direction starting from the reference direction, $\hat{s}$. WSS values are shown for each rosette in magenta. Filled circles are also indicated corresponding to points representing the maximum acceleration (red), deceleration (blue), and mean value of WSS (black) in each rosette. Tabulated values show

the relevant flow metrics at these locations. Changes in the WSS magnitude and direction at point ~~H~~ B (Figure 4b) are due to strong secondary flows (Krishna *et al,* 2017). The various shear metrics are indicated for this rosette. TAWSS is calculated as the time average of the WSS magnitude and represents the average length of the arrows in the shear rosette. Because TAWSS is a time averaged quantity, a higher weightage is given to WSS values that occur over longer time durations. The mean shear stress (meanWSS) is the time average of the WSS vector~~, indicated with a magenta circle~~ (Figure 4b) and is not at the rosette centroid because ~60% of the cardiac cycle (Figure 2a) relates to the dwell phase (shown using black in the figure 4) when flow rate and WSS values are very small (meanWSS~1.36 Pa, and TAWSS ~1.71 Pa).

OSI relates oscillations in WSS about the origin along one direction (=0.09 for this case) and does not reflect the presence of the disturbed flows (Ku *et al* 1985; Andersson *et al* 2017). A rosette that does not enclose the origin has an OSI =0 even though there may be large variations in the WSS. The corresponding transWSS metric (=0.83), defined as the time-averaged value of the transverse component of the WSS vector, is based on flow bi-directionality and is related to the width of the rosette when the principal direction is in the direction of mean shear stress (Table I). For flows with 0 mean WSS vector, such as in purely oscillatory flows, purely circular flows, or where the dominant flow is oscillatory, transWSS gives artefactual values (Peiffer *et al,* 2013). Morbiducci and coworkers defined the R measure as averaged ratio of the WSS in the secondary and axial directions over the cardiac cycle (Morbiducci *et al*, 2015). Because this measure is an averaged quantity, it may not give a complete description of the flow bidirectionality. An alternate metric to capture WSS bidirectionality is the anisotropic ratio (AR) which is calculated by taking the ratio of projections of the shear rosette along the minor to the major axes,

$$AR = \frac{\tau_{2(max)} - \tau_{2(min)}}{\tau_{1(max)} - \tau_{1(min)}} = \frac{L_2}{L_1} \quad (1)$$

AR is the ratio of the width to length of the rosette along the principal directions. AR has a value of 0 for unidirectional flows and 1 for equibiaxial flows. AR=0.81 for the rosette in Figure 4b.

Figures 4c and 4d show rosettes at points ~~G~~ A and ~~I~~ C (Figure 1a) along with values of relevant flow metrics. The flow is symmetric about the medial plane where secondary flows are absent. There are marked differences in the rosette shapes as we traverse from the outer to the inner wall for a given transverse plane. The maximum bidirectionality is at ~ $\phi = 135°$ (Figure 4b) where the secondary flow is the strongest. At $\phi = 45^o$, the secondary flows are significantly weaker which results in a smaller rosette. The various shear metrics are hence correspondingly smaller as compared to the rosette in Figure 4b. The shear rosette at $\phi = 180^o$(point I) corresponds to a unidirectional, oscillatory flow, thus AR and transWSS values are both zero. Because of shear stress reversals, the OSI value is high (=0.48) and is close to the maximum possible value of 0.5. The low flow rates during the diastolic phase lead to small values of WSS at these locations.

3.3 Flow metrics in the control ICA and patient specific geometry of ICA with aneurysm

The flow in the control ICA is mainly quasi-steady and unidirectional in the absence of branches and other geometric distortions due to aneurysms etc. Secondary flow, caused by curvature, is however generally present. Figure 5a show streamlines at peak velocity in a control geometry of ICA which includes regions with curvatures ranging from 0.3-0.7. Although, the average velocities in the ICA are similar in magnitude to those in the AA, the WSS is significantly higher. Helical streamlines clearly show the presence of both axial and secondary components of velocity. Secondary flow is clearly visible in the transverse cross-section (Figure 5b) at point D corresponding to the point of high curvature where WSS value is the maximum. We note that this flow is different from Dean's flow where we clearly see the presence of two vortices with flow in the core moving radially outward (Berger *et al,*

1983). The shear rosette corresponding to this point demonstrates the unidirectional nature of flow with significantly higher WSS variations as compared to those seen for AA (Figure 4). Because the flow is unidirectional and the velocity magnitude is proportional to the flow rate at that time, the shear rosettes lie nearly along straight lines. The TAWSS value at this point (Table II) is lower than the rosette centroid value due to the low stress values which occur over longer time durations when the flow rates are small.

The quasi-steady flow in control ICA makes the shear rosettes very different from those in control AA. Stress rosettes at the other three locations (Figure 5c-f) show varying magnitudes of mean and fluctuations in the WSS in addition to indicating the unidirectional flows. At point C, WSS is along θ=315° which indicates similar contributions from the axial and secondary components. The rosettes for ICA show significantly higher values of WSS as compared to AA. Because the rosettes do not cross the origin, the OSI values are zero at all these locations. The AR and transWSS values are low in the control ICA in comparison to the control AA due to the unidirectional flows in the ICA.

Flows in patient specific geometries are more complicated due to changing cross-sections and the presence of branches that result in larger TAWSS variations. ICA with aneurysm (Figure 6) has shear rosettes with irregular shapes as compared to AA. Rosettes have nearly straight lines except at few locations that show some bi-directionality (e.g. points A and C); the flow is nearly unidirectional at points B, D, and E. Figure 6d shows several reversals in the transverse component of WSS about the principal axis. Within the aneurysm, WSS values are low due to low velocities. In contrast, high values of WSS are seen downstream of the aneurysm due to vessel lumen narrowing. The curvatures in the complex patient specific ICA geometry model were in the similar range ($0.3 \leq \beta \leq 0.7$) as the control ICA geometry. However, the patient specific complex geometry shows higher values of TAWSS, additional shear reversals, and the presence of shear stress bi-directionality as

compared to control ICA. These factors may be causally linked to mechanobiological processes that ultimately lead to aneurysm rupture or stability in these vessels.

3.4 Spatial distributions of flow metrics for control and patient specific geometries of aorta

Spatial distributions of flow metrics (TAWSS, OSI, AR and transWSS) are shown for the control AA and ICA in addition to patient specific geometries of AA and ICA in Figure7. The regions of high OSI values, just downstream of the curved section in the AA geometry, are correlated with regions of low TAWSS where the flow is likely to be highly disturbed. There is hence little correspondence between the distributions of OSI and transWSS metrics. OSI has been widely used to explore pulsatility effects of the flow (Ku *et al* 1985) and relate them to mass transport ~~(Ku *et al* 1985)~~ (Arzani et.al, 2017). The OSI is related to WSS fluctuation about the origin in the rosette and relates neither to the amplitude of WSS fluctuations nor the flow bi-directionality. Large OSI values are linked to changes in the WSS vector that induces mass accumulation; low OSI correlates with regions that have smaller changes in the WSS vector.

Regions of elevated AR in the control AA geometry correspond to regions where the secondary flows are high (points B, E, H in Figure 1a; Figure 5). There are no secondary flows in straight sections of tubes where AR = 0. AR and transWSS account for flow bidirectionality, and values of these metrics are higher in curved sections of the patient specific AA geometry due to presence of secondary flows (Figure 7).

Many locations in the ICA with aneurysm have TAWSS values > 10 that appear red in the figure. In most locations, the AR values are low. In contrast to the control ICA, the AR values are higher for the ICA with aneurysm and the flows are more bi-directional. The transWSS metric is similar to AR since both metrics are related to the transverse component of WSS. However, transWSS measures only the component perpendicular to the mean shear stress vector and is dimensional. In contrast, AR is a non-dimensional quantity that is a direct

measure of bidirectionality. For example, the large magnitude of WSS over the cardiac cycle is responsible for the relatively high transWSS in regions where the secondary flows are present although the rosette has low bi-directionality.

Shear rosette descriptions at critical locations, identified from spatial distributions of the different metrics (example Figure 7), are essential in linking the flow physics to the underlying endothelial mechanobiology. The endothelial cell monolayer provides a direct link between fluid stress and the vessel wall constituents. EC morphology is elongated in the direction of flow under unidirectional flow conditions (Davies *et al,* 1984; Chien, 2007; Chiu and Chien, 2011; Baeyens and Schwartz, 2016). Disturbed blood flows, caused by flow recirculation, separations, and other phenomena, play a critical role in vascular homeostasis through changes to the gene expression levels of various atherogenic and thromogenic signaling molecules in the EC monolayer. These changes are shown to enhance endothelial turnover and modulate smooth muscle cell migrations in the arterial wall (Langille and O'Donnell, 1986; Cheng *et al*, 2006; Chiu and Chien, 2011). Cellular morphology alters to a less organized one with near-polygonal shapes in regions of disturbed flows that induce and sustain the activation of several atherogenic genes (Davies, 1995; Chiu and Chien, 2011). Ku and coworkers were among the earliest researchers to explore the correlations between atherosclerosis-prone regions in arteries with disturbed flows (Ku *et al*, 1985). ECs do not show their characteristic elongated phenotype in atheroprone regions which suggests a causal role for cellular alignment in modulating inflammatory pathways. Based on these studies, they hypothesized the importance of oscillatory shear reversals in plaque formation. In vitro studies of perpendicular flows to aligned EC monolayers shows an increase in inflammatory pathways as compared to flows in the aligned cell orientations that have anti-inflammatory signaling (Wang *et al*, 2013). The transverse component of WSS may hence play a dominant role in plaque formation rather than WSS oscillations (Peiffer *et al*., 2013; Mohamied *et al*.,

2015). Multidirectional flow metrics, including DOSI, transWSS, and decomposition of WSS along the axial and secondary directions, have been used to characterize regions of disturbed flow dynamics and linked to endothelial monolayer permeability, inflammatory markers, and remodeling (Chakraborty *et al,* 2012; Peiffer *et al,* 2013; Morbiducci *et al,* 2015; Dabagh *et al,* 2017). Changes in the flow dynamics near the wall affects species transport and increases cell permeability. These lead to increased leucocyte transmigration in the wall and a subsequent degradation of the extracellular matrix (Wilson *et al,* 2012; Babu *et al,* 2015; Arzani and Shadden, 2016; Dabagh *et al,* 2017). Experimental studies show that the dominant principal flow direction is a better predictor of cellular alignment under bidirectional flows; EC align to minimize the shear stress along the transverse axis (Ghim *et al,* 2017; Chakraborty *et al,* 2012). Mechanosensors that are hypothesized to mediate the endothelial response to shear stress include the endothelial glycocalyx, G protein-coupled receptors, ion channels, adherens junctions and integrin-mediated cell–matrix adhesions (Chiu and Chien, 2011; Baeyens *et al*, 2014; Peiffer *et al.*, 2013). Recent studies show the importance of a transmembrane proteoglycan, syndecan-4, in the directional mechano-sensing adaption response of ECs (Baeyens *et al*, 2014). The specific mechanisms of directional WSS sensing by EC and their links to plaque formation are, however, presently unknown. Shear rosettes give detailed information of the flow dynamics allowing links between mechanics and biology.

4. Conclusions

We compared the distributions of TAWSS, OSI, and transWSS in control and patient specific geometries of AA with aneurysm and the ICA with aneurysm. We use a shear rosette representation to give a complete and immediate picture of the variations in the WSS over a cardiac cycle. Most existing metrics can be immediately assessed using the rosette geometric properties. The rosette centroid is related to the mean WSS, splay about the origin gives the

OSI values, it's width yields an estimate of transWSS value when the principal direction is in the direction of mean shear stress, and the ratio of the length to the width of the rosette gives the AR. TAWSS gives the time average of the WSS alone but does not characterize the temporal variations of magnitude and direction of WSS which occur during the cardiac cycle. OSI captures the pulsatility during the cardiac cycle only when the WSS values cross the origin and also does not account for the flow bidirectionality. The AR metric proposed in this study is a direct measure of the ratio of the two transverse components when resolved along the principal directions. The transWSS and AR metrics capture the bi-directional nature of the flow and hence yield similar distributions in the geometries considered in our study. However, in contrast to transWSS, AR is a direct measure of bidirectionality, is bounded between 0 and 1, and is non-dimensional. The shear rosette is a more fundamental and complete representation of the flow dynamics in arteries and may be used to better assess the correlation between WSS and EC morphologies.

5. Acknowledgements

We thank Amartya Gupta for help with geometry reconstruction of the ICA reported in this study. NG acknowledges financial support from the Department of Biotechnology (BT/PR13926/MED/31/97/2010). PW acknowledges financial support from UK EPSRC (EP/N014642/1). PW and NG thank joint funding through the Department of Science and Technology-UKIERI (DST/INT/UK/P-68/2014).

6. Conflict of interest statement

None of the authors have any conflicts of interests to declare regarding the submission.

7. Appendix A. Patient specific models of arteries

CT images were acquired before the surgical repair and the vessel geometries were extracted using Mimics 10.01 (Materialise, Leuven, Belgium). The CT data has voxel dimensions of 1.24 x 1.24 x 0.789 mm^3. The images were segmented to isolate the aorta and bones from the surrounding soft tissue, and a region growing algorithm was used to create a mask for reconstructing the 3D model. The mask was truncated above the coronary arteries and in the region below the descending aorta above the renal arteries. The Branchiocephalic Artery (BCA), the Left Common Carotid Artery (LCCA), and the Left Subclavian Artery (LSA), and all other intercoastal arteries were truncated; the latter accounts for less than 1% of the blood flow (Olufsen *et al* 2000). In addition, the BCA, LCCA and LSA were clipped where the BCA splits into the right common carotid artery and the right subclavian artery. This cropped mask was used to construct the initial 3D geometry as an STL file using contour interpolation between the CT scanned slices. Finally, each clipped branch was extended in length by approximately one diameter. The inlet of the curved section was about 8 diameters in length and the outlet was 4 diameters in length. Because the chosen inlet length was $>$ $\int_0^T U_i(t)dt$, we expect the presence of fully developed flows in the curved section.$U_i(t)$ is the area averaged axial velocity and T the time period of the cardiac cycle. The full extended lengths at the inlet and outlet of the control AA used in the computation are not shown in Figure 1a. Figure 1b shows the AA geometry with aneurysm before surgery.

In addition to the AA geometry, we used a realistic model (patient id: C0088b) of ICA, available at open-source aneurisk database, that was reconstructed with constant

diameter from the centreline coordinates of the artery (Aneurisk-Team, 2012). The sub-branches were removed, and the inlet and outlet sections were added similar to the procedure for the control AA model. The final geometry had curvatures in multiple planes with no sub-branches with a length of 72 mm from the inlet and served as a control ICA geometry (Figure 1c). The maximum curvature ratio was ~0.7 in the control geometry of the ICA. We also selected the geometry of a patient with sidewall intracranial aneurysm (Figure1d) using the European @neurIST project (Villa-Uriol *et al,* 2011, Chen *et al,* 2013). Typical Re, α and Dean's numbers in the AA are ~3000, 34 and ~1900 whereas these are ~450, 3 and ~400 for the ICA. The values of β for the AA are ~0.38 and range from 0.3-0.7 in the ICA.

Reconstructed geometries were imported into ANSYS® ICEM CFD 13.0 (ANSYS Inc., Canonsburg, Pennsylvania) and unstructured meshes for the control geometries were created that contained hexahedral elements. ~~The realistic~~ Patient specific AA and ICA geometries also contained tetrahedral elements. A finer mesh using prism layers was used to resolve the unsteady boundary layer ($\delta \sim \sqrt{\nu T}$; where ν is the kinematic viscosity of blood and T is the time period of the cardiac cycle) in all the different geometries. The boundary layer consisted of 20 prism layers with a first length of 14 μm that corresponded to the distance of first cell from the wall; subsequent cell sizes increased with growth rate of 1.2. The boundary layer mesh hence transitioned uniformly into the core mesh. The total number of elements were 2,691,000 in the AA control, 5,883,547 for the patient specific AA with aneurysm, 2,362,320 elements for the control ICA, and 3,705,990 elements for the patient specific ICA with aneurysm.

The governing Navier-Stokes equations were solved using a commercial finite-volume based solver (ANSYS® FLUENT 13.0). Transient terms were integrated using a second order implicit method. A second order upwind scheme was used to discretize the convection terms, and the diffusion terms were central differenced to be accurate in their

second order. We use SIMPLEC algorithm for pressure velocity coupling and the flow was assumed to be laminar within the domain (Mohamied *et al,* 2017, Vasava *et al,* 2011). We did not include turbulence models in the AA cases as the flows are unsteady and do not become fully turbulent. Grid and flow cycle independence were not achieved for the patient specific AA geometry with aneurysm. (need to write something here to wrap up) ~~The chosen time step was 10^{-3} s and the criterion for convergence for residuals was set below 10^{-5} for each of the continuity and the three velocity components in each case. Grid independence studies were carried out based on the following criterion: the RMS difference of WSS between successive meshes was less than 2% of the RMS of the WSS over one cardiac cycle. The number of cells were doubled until this criterion was met. Flow cycle independence was also checked until the shear rosettes were time periodic to eliminate the initial transient effects. Four cardiac cycles were simulated and results corresponding to the last cycle are reported in this study.~~

8. Appendix B. Principal directions in the shear rosette

The rosette is represented using an orthogonal set of coordinates, $\hat{\boldsymbol{s}}$ and $\hat{\boldsymbol{b}}$, which are the axial and secondary flow directions respectively. Let '1' and '2' represent the two principal directions, $\boldsymbol{\theta}$ be the angle between the instantaneous shear stress vector $\boldsymbol{\tau}$ and $\hat{\boldsymbol{s}}$, and $\boldsymbol{\phi}$ be the angle between the directions '1' and $\hat{\boldsymbol{s}}$. $\boldsymbol{\tau_1}$ is the projection of $\boldsymbol{\tau}$ on direction 1 and $\boldsymbol{\tau_2}$ is the projection on direction 2. By definition (Chakraborty *et al.*, 2012),

$$\int_0^T \boldsymbol{\tau}_1 \boldsymbol{\tau}_2 \, dt = 0 \tag{1}$$

where T is the time period of the cardiac cycle. and τ_{mag} is the magnitude of the $\boldsymbol{\tau}$. We show that the above relation is equivalent to either maximizing $\int_0^T \boldsymbol{\tau}_1^2 \, dt$ in one principal direction and minimizing $\int_0^T \boldsymbol{\tau}_2^2 \, dt$ in the other principal direction, "2". We compute the principal directions from the shear stress distributions.

$$\boldsymbol{\tau}_1(t) = \boldsymbol{\tau}_{mag} cos\,(\theta(t) - \phi) \tag{2}$$

$$\boldsymbol{\tau}_2(t) = \boldsymbol{\tau}_{mag} sin\,(\theta(t) - \phi) \tag{3}$$

$$\boldsymbol{\tau}_{mag}^2 = \boldsymbol{\tau}_1^2 + \boldsymbol{\tau}_2^2 \tag{4}$$

Substituting in equation 1, we get,

$$\int_0^T \boldsymbol{\tau}^2{}_{mag}(t)\, sin\left(2(\theta(t) - \phi)\right) dt = 0 \tag{5}$$

Because ϕ is an independent variable, we can rewrite this expression as a maximization or a minimization problem as:

$$\tfrac{1}{2}\tfrac{\partial}{\partial \phi}\left(\int_0^T \boldsymbol{\tau}_{mag}^2(t)\cos(2(\theta(t) - \phi))\, dt\right) = 0 \tag{6}$$

Thus, the integral in the above expression reaches an extremum at a particular value of ϕ which gives the principal directions. The integral in equation (6) can be rewritten as,

$$I = \int_0^T \left(\boldsymbol{\tau}_{mag}^2(t)\cos^2(\theta(t) - \phi) \; - \boldsymbol{\tau}_{mag}^2 \sin^2(\theta(t) - \phi)\right) dt \tag{7}$$

Using equations (2-4), we get

$$I = \int_0^T \left(\boldsymbol{\tau}_1^2(t) - \boldsymbol{\tau}_2^2(t)\right) dt \quad (8)$$

$$I = \int_0^T \left(\boldsymbol{\tau}_{mag}^2(t) - 2\boldsymbol{\tau}_2^2(t)\right) dt \quad (9)$$

$$I = \int_0^T \left(2\boldsymbol{\tau}_1^2(t) - \boldsymbol{\tau}_{mag}^2(t)\right) dt \quad (10)$$

Because $\boldsymbol{\tau_{mag}(t)}$ is independent of the choice of reference direction,

$$\int_0^T \boldsymbol{\tau}_{mag}^2(t)\, dt = const \quad (11)$$

This procedure takes into account the time spent by the WSS vector at each location over the cardiac cycle.

9. References

Andersson, M., Lantz, J., Ebbers, T., & Karlsson, M. 2017. Multidirectional WSS disturbances in stenotic turbulent flows: A pre-and post-intervention study in an aortic coarctation. Journal of Biomechanics, *51*, 8-16.

Aneurisk-Team 2012. '{AneuriskWeb project website}, http://ecm2.mathcs.emory.edu/aneuriskweb'. Available at: http://ecm2.mathcs.emory.edu/aneuriskweb.

Aparicio, P., Mandalsti, A., Boamah, J., Chen, H., Selimovic, A., Bratby, M., Uberoi, R., Ventikos, Y., Watton, P.N. 2014. Modelling the influence of endothelial heterogeneity on progression of arterial disease: Application to abdominal aortic aneurysm evolution. International Journal of Numerical Methods in Biomedical Engineering 30(5), 563-583.

Arzani, A., Gambaruto, A.M., Chen, G., Shadden, S.C. 2016. Lagrangian wall shear stress structures and near-wall transport in high-Schmidt-number aneurysmalflows. Journal of Fluid Mechanics 790, 158–172.

Arzani, A. and Shadden, S.C. 2016. Characterizations and correlations of wall shear stress in aneurysmal flow. Journal of Biomechanical Engineering 138,14503.

Arzani, A., Gambaruto, A.M., Chen, G., Shadden, S.C.2017. Wall shear stress exposure time: a Lagrangian measure of near-wall stagnation and concentration in cardiovascular flows. Biomechanics and Modeling in Mechanobiology 16,787-803.

Arzani, A. and Shadden, S.C.2018. Wall shear stress fixed points in cardiovascular fluid mechanics. Journal of Biomechanics 73,145-152.

Asakura, T. and Karino, T. 1990. Flow patterns and spatial distribution of atherosclerotic lesions in human coronary arteries. Circulation Research 66, 1045–1066.

Babu, A.R., Byju, A.G. and Gundiah, N.2015. Biomechanical properties of human ascending

thoracic aortic dissections. Journal of Biomechanical Engineering 137, 81013.

Baeyens, N., Bandyopadhyay, C., Coon, B. G., Yun, S., & Schwartz, M. A. 2016. Endothelial fluid shear stress sensing in vascular health and disease. The Journal of Clinical Investigation, 126(3), 821-828.

Baeyens, N. and Schwartz, M.A. 2016. Biomechanics of vascular mechanosensation and remodeling. Molecular biology of the Cell. 7–11.

Berger, S. A., Talbot, L. and Yao, L. S. 1983 Flow in curved pipes. Annual Reviews of Fluid Mechanics 15, 461–512.

Berger, S.A., Goldsmith, W. and Lewis, E.R. 1996. Introduction to Bioengineering. Oxford University Press, USA.

Bulusu, K.V. and Plesniak, M.W. 2013. Secondary flow morphologies due to model stent-induced perturbations in a 180° curved tube during systolic deceleration. Experiments in Fluids 54, 1–13.

Caro, C.G., Fitz-Gerald, J.M. and Schroter, R.C. 1971. Atheroma and arterial wall shear observation, correlation and proposal of a shear dependent mass transfer mechanism for atherogenesis. Proceedings of the Royal Society, London B: Biol. Science. 177,109–133.

Chakraborty, A., Chakraborty, S., Jala, V. R., Haribabu, B., Sharp, M. K., & Berson, R. E. 2012. Effects of biaxial oscillatory shear stress on endothelial cell proliferation and morphology. Biotechnology and Bioengineering, 109(3), 695-707.

Chandran, K.B. and Yearwood, T.L. 1981. Experimental study of physiological pulsatile flow in a curved tube. Journal of Fluid Mechanics111,59–85.

Chatzizisis, Y. S., Coskun, A. U., Jonas, M., Edelman, E. R., Feldman, C. L., & Stone, P. H. 2007. Role of endothelial shear stress in the natural history of coronary atherosclerosis and vascular remodeling: molecular, cellular, and vascular behavior. Journal of the American College of Cardiology, 49(25), 2379-2393.

Chen, H., Selimovic, A., Thompson, H., Chiarini, A., Penrose, J., Ventikos, Y., & Watton, P. N. 2013. Investigating the influence of haemodynamic stimuli on intracranial aneurysm inception. Annals of Biomedical Engineering, 41(7), 1492-1504.

Chien, S. 2007. Mechanotransduction and endothelial cell homeostasis: the wisdom of the cell. American Journal of Physiology, Heart and Circulatory Physiology 292, H1209-H1224.

Chiu, J.J. and Chien, S. 2011. Effects of disturbed flow on vascular endothelium: pathophysiological basis and clinical perspectives. Physiological Reviews 91, 327–387.

Dabagh, M., Jalali, P., Butler, P. J., Randles, A., & Tarbell, J. M. 2017. Mechanotransmission in endothelial cells subjected to oscillatory and multi-directional shear flow. Journal of the Royal Society Interface, 14(130), 20170185.

Davies, P. F., Dewey, C. F., Bussolari, S. R., Gordon, E. J., & Gimbrone, M. A. 1984. Influence of hemodynamic forces on vascular endothelial function. In vitro studies of shear stress and pinocytosis in bovine aortic cells. The Journal of clinical investigation, 73(4), 1121-1129.

Davies, P.F. 1995. Flow-mediated endothelial mechanotransduction. Physiological Reviews 75,519–560.

Ghim, M., Alpresa, P., Yang, S. W., Braakman, S. T., Gray, S. G., Sherwin, S. J., van Reeuwijk, M. & Weinberg, P. D. 2017. Visualization of three pathways for macromolecule transport across cultured endothelium and their modification by flow. American Journal of Physiology-Heart and Circulatory Physiology, 313(5), H959-H973.

Glenn, A. L., Bulusu, K. V., Shu, F., & Plesniak, M. W. 2012. Secondary flow structures under stent-induced perturbations for cardiovascular flow in a curved artery model. International Journal of Heat and Fluid Flow, *35*, 76-83.

Hamakiotes, C.C. and Berger, S.A. 1988. Fully developed pulsatile flow in a curved pipe. Journal of Fluid Mechanics195, 23–55.

He, X.J. and Ku, D.N. 1996. Pulsatile flow in the human left coronary artery bifurcation: Average conditions. Journal of Biomechanical Engineering 118, 74–82. doi: 10.1115/1.2795948.

Ho, H., Suresh, V., Kang, W., Cooling, M. T., Watton, P. N., & Hunter, P. J. 2011. Multiscale modeling of intracranial aneurysms: cell signaling, hemodynamics, and remodeling. IEEE Transactions on Biomedical Engineering, 58(10), 2974-2977.

Jarrahi, M., Castelain, C. and Peerhossaini, H. 2011. Laminar sinusoidal and pulsatile flows in a curved pipe. Journal of Applied Fluid Mechanics 4,21–26.

Komai, Y. and Tanishita, K. 1997. Fully developed intermittent flow in a curved tube. Journal of Fluid Mechanics 347,263–287.

Krishna, C.V., Gundiah, N. & Arakeri, J.H. 2017. Separations and secondary structures due to unsteady flow in a curved pipe. Journal of Fluid Mechanics 815, 26–59.

Ku, D. N., Giddens, D. P., Zarins, C. K., & Glagov, S. 1985. Pulsatile flow and atherosclerosis in the human carotid bifurcation. Positive correlation between plaque location and low oscillating shear stress. Arteriosclerosis: An Official Journal of the American Heart Association, Inc., 5(3), 293-302.

Ku, D.N. 1997. Blood flow in arteries. Annual Review of Fluid Mechanics 29, 399–434.

Kulcsár, Z., Ugron, A., Marosfői, M., Berentei, Z., Paál, G., & Szikora, I. 2011. Hemodynamics of cerebral aneurysm initiation: the role of wall shear stress and spatial wall shear stress gradient. American Journal of Neuroradiology, 32 (3), 587-594.

Malek, A.M., Alper, S.L. and Izumo, S. 1999. Hemodynamic shear stress and its role in atherosclerosis. JAMA 282, 2035–2042.

Mantha, A., Karmonik, C., Benndorf, G., Strother, C., & Metcalfe, R. 2006. Hemodynamics in a cerebral artery before and after the formation of an aneurysm. American Journal of Neuroradiology, 27(5), 1113-1118.

Mohamied, Y., Sherwin, S.J. and Weinberg, P.D. 2017. Understanding the fluid mechanics behind transverse wall shear stress. Journal of Biomechanics 50, 102–109.

Morbiducci, U. *et al* 2015. A rational approach to defining principal axes of multidirectional wall shear stress in realistic vascular geometries, with application to the study of the influence of helical flow on wall shear stress directionality in aorta. Journal of Biomechanics 48, 899–906.

Olufsen, M. S., Peskin, C. S., Kim, W. Y., Pedersen, E. M., Nadim, A., & Larsen, J. (2000). Numerical simulation and experimental validation of blood flow in arteries with structured-tree outflow conditions. Annals of Biomedical Engineering, *28*(11), 1281-1299.

Peiffer, V., Sherwin,S.J. and Weinberg, P.D. 2013. Computation in the rabbit aorta of a new metric the transverse wall shear stress to quantify the multidirectional character of disturbed blood flow. Journal of Biomechanics 46, 2651–2658.

Peiffer, V., Sherwin, S.J. and Weinberg, P.D. 2013. Does low and oscillatory wall shear stress correlate spatially with early atherosclerosis? A systematic review. Cardiovascular Research, 99,242–250.

Penn,D.L., Komotar, R.J. and Connolly, E.S. 2011 Hemodynamic mechanisms underlying cerebral aneurysm pathogenesis. Journal of Clinical Neuroscience 18, 1435–1438.

Potter, C. M., Lundberg, M. H., Harrington, L. S., Warboys, C. M., Warner, T. D., Berson, R. E., Moshkov, A.V., Gorelik, J., Weinberg, P.D. and Mitchell, J. A. (2011). Role of shear stress in endothelial cell morphology and expression of cyclooxygenase isoforms. Arteriosclerosis, Thrombosis, and Vascular Biology, 31(2), 384-391.

Rachev, A. 2000. A model of arterial adaptation to alterations in blood flow', Journal of Elasticity 61, 83–112.

Reymond, P., Merenda, F., Perren, F., Rufenacht, D., & Stergiopulos, N. (2009). Validation of a one-dimensional model of the systemic arterial tree. American Journal of Physiology-Heart and Circulatory Physiology, 297(1), H208-H222.

Robertson, A.M. and Watton, P.N. 2012. Computational fluid dynamics in aneurysm research: critical reflections, future directions. America Journal of Neuroradiology 33, 992–995.

Selimovic, A., Ventikos, Y., Watton, P.N. 2014. Modelling the evolution of cerebral aneurysms: Biomechanics Mechanobiology and multiscale modelling. Proceedings of the 23rd International Congress on Theoretical and Applied Mechanics 10, 396-409.

Sudo, K., Sumida, M. and Yamane, R.1992. Secondary motion of fully developed oscillatory flow in a curved pipe. Journal of Fluid Mechanics 237, 189–208.

Suo, J., Ferrara, D. E., Sorescu, D., Guldberg, R. E., Taylor, W. R., & Giddens, D. P. (2007). Hemodynamic shear stresses in mouse aortas: implications for atherogenesis. Arteriosclerosis, Thrombosis, and Vascular Biology, 27(2), 346-351.

Talbot, L. and Gong, K.O. 1983. Pulsatile entrance flow in a curved pipe. Journal of Fluid Mechanics 127, 1–25.

Timité, B., Castelain, C. and Peerhossaini, H. 2010. Pulsatile viscous flow in a curved pipe: Effects of pulsation on the development of secondary flow. International Journal of Heat Fluid Flow 31, 879–896.

Topper, J.N. and Gimbrone, Jr M.A. 1999. Blood flow and vascular gene expression: fluid shear stress as a modulator of endothelial phenotype. Molecular Medicine Today 5, 40–46.

Villa-Uriol, M. C., Berti, G., Hose, D. R., Marzo, A., Chiarini, A., Penrose, J Pozo, J., Schmidt, J.G., Singh, P., Lycett, R., Larrabide, I.& Frangi, A.F. 2011. @ neurIST complex information processing toolchain for the integrated management of cerebral aneurysms. Interface Focus, 1(3), 308-319.

Wang, C., Baker, B. M., Chen, C. S., & Schwartz, M. A. 2013. Endothelial cell sensing of flow direction. Arteriosclerosis, Thrombosis, and Vascular Biology, 33(9), 2130-2136.

Wilson, J.S., Baek, S. and Humphrey, J.D. 2012. Importance of initial aortic properties on the evolving regional anisotropy, stiffness and wall thickness of human abdominal aortic aneurysms. Journal of Royal Society Interface rsif20120097.

Yearwood, T.L. and Chandran, K.B. 1982. Physiological pulsatile flow experiments in a model of the human aortic arch. Journal of Biomechanics 15, 683–704.

Zarins, C. K., Giddens, D. P., Bharadvaj, B. K., Sottiurai, V. S., Mabon, R. F., & Glagov, S. 1983. Carotid bifurcation atherosclerosis. Quantitative correlation of plaque localization with flow velocity profiles and wall shear stress. Circulation Research, 53(4), 502-514.

10. List of Figures

Figure 1: Geometries of the arterial vessels used in CFD simulations are shown for (a) AA (control) with 180°curved section (2a = 32 mm, β=0.38). (b) patient specific geometry of AA with aneurysm, and (c) Control case of ICA reconstructed from aneurisk database (Aneurisk-Team, 2012), and (d) patient specific geometry of ICA with aneurysm.

Figure 2: Inlet flow rate waveforms which were used in CFD simulations are indicated. (a) Input waveforms for AA is shown along with flow ~~rates~~ in the branches with the corresponding waveform for (b) ICA. The acceleration phase is marked in red and deceleration phase is marked in blue. The inlet flow rate in the diastolic phase is marked in black; the maximum acceleration and deceleration points are indicated using a cross. Filled circles correspond to the maximum acceleration (red) and deceleration (blue) points.

Figure 3: Velocity contours with superimposed velocity vectors in the medial and three transverse planes are shown for the control AA geometry. The full extended lengths at the inlet and outlet used in the computation are not shown. The three transverse planes, labelled as P45, P90, and P135, are 45°, 90°, and 135° respectively from the inlet. Results are shown at two time points of the cardiac cycle corresponding to (a) peak velocity of systole (t = 0.14 s), and (b) end of systole (t = 0.35 s), which are shown with a black cross in Figure 2. Collision of the secondary flows in the medial plane causes a radially outward propagating jet and a pair of vortices.

Figure 4: Shear rosettes show variations in shear stresses over one cardiac cycle for the accelerating (red), decelerating (blue), and stop phase of the cycle (black) for (a) AA control at point B in Figure 1a. The two perpendicular black lines are the principal directions of the rosette marked as $\hat{s}$ and $\hat{b}$, shown in the figure, that correspond to the axial and secondary flow directions. Angular positions are marked at every 30^o in the anticlockwise direction

starting from the reference direction, $\hat{s}$ (b) The shear rosette is shown for ~~the same~~ point B with the mean WSS, transWSS, and AR metrics given by points marked on the rosette. (c) Rosettes are shown at point A marked on plane P45 and (d) Point C marked on plane P45. WSS values are shown for each rosette in magenta. Points corresponding to the maximum acceleration (red), deceleration (blue), and mean value of WSS (black) are indicated using filled circles. Values of the relevant flow metrics at these locations are also shown.

Figure 5: (a) Streamlines, corresponding to the peak velocity, are shown for the control ICA. (b) Axial velocity contours with superimposed velocity vectors are shown for the highlighted plane. (c-f) Shear stress rosettes are plotted corresponding to the points A-D marked in (a).

Figure 6: Streamlines are shown for the ICA with aneurysm. Shear stress rosettes are plotted at points (A-E) indicated on the surface.

Figure 7: TAWSS, OSI, AR, transWSS metrics are plotted for (a) control, (b) patient specific AA geometry with aneurysm, (c) Control ICA, and (d) patient specific model of ICA with aneurysm.

11. List of Tables

Table I: Definitions and a brief description of select shear metrics in this study.

Table II: Values of the different shear metrics for control ICA geometry and patient specific ICA with aneurysm are given at selected points in Figure 5 and Figure 6.

Figure 1

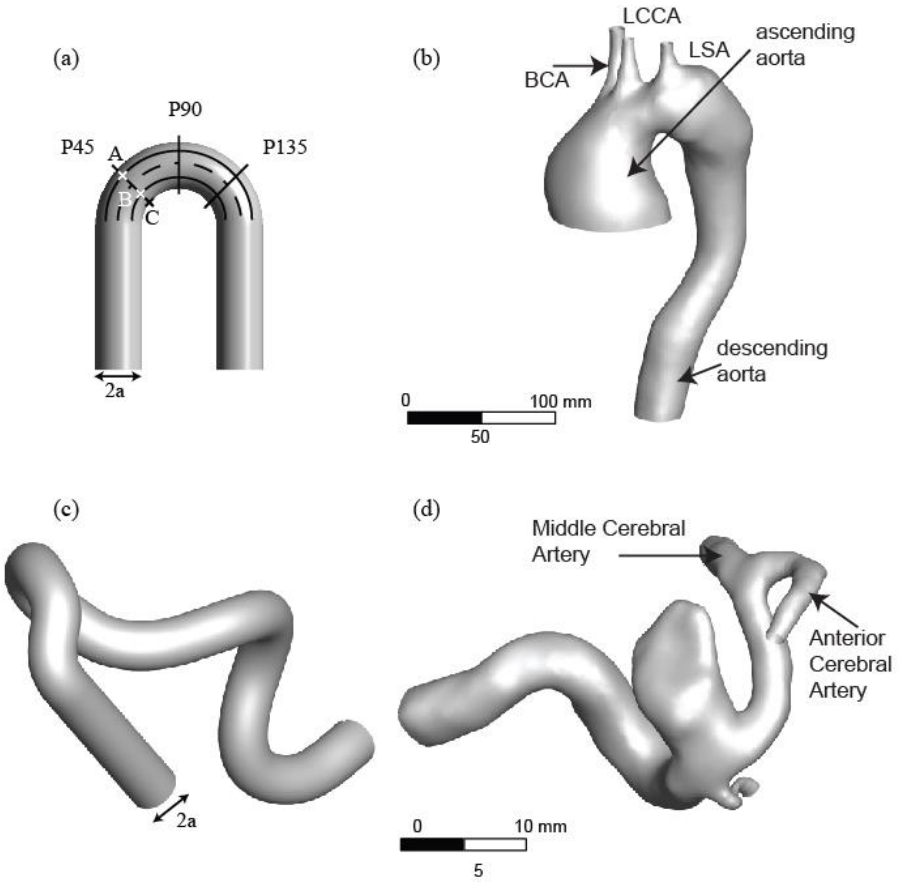
(a)
P90
P45
A
P135
B
C
2a
(b)
LCCA
LSA
ascending
aorta
BCA
descending
aorta
0
100 mm
50
(c)
2a
(d)
Middle Cerebral
Artery
Anterior
Cerebral
Artery
0
10 mm
5

Figure 2

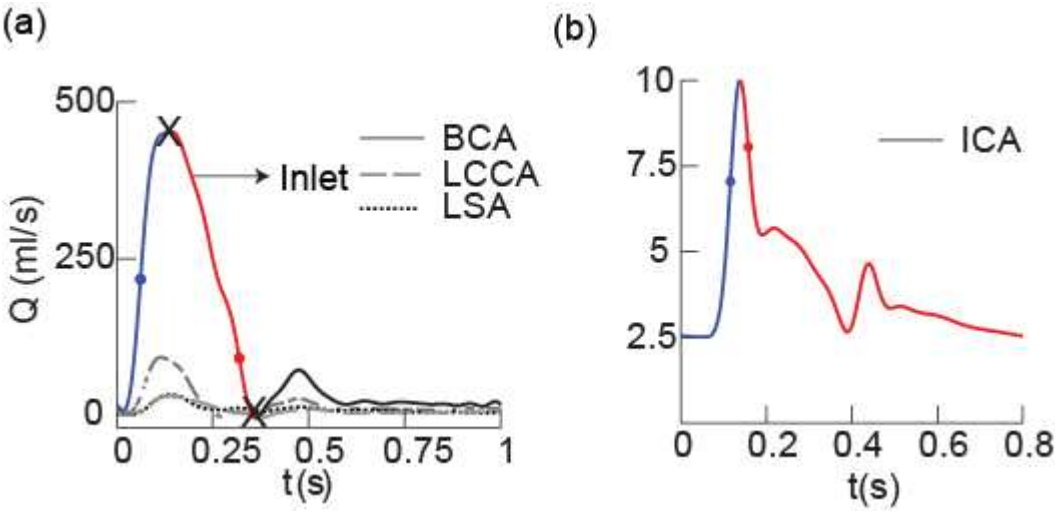
(a)
500
250
0
Q (ml/s)
Inlet
BCA
LCCA
LSA
0
0.25
0.5
0.75
1
t(s)
(b)
10
7.5
5
2.5
ICA
0
0.2
0.4
0.6
0.8
t(s)

Figure 3

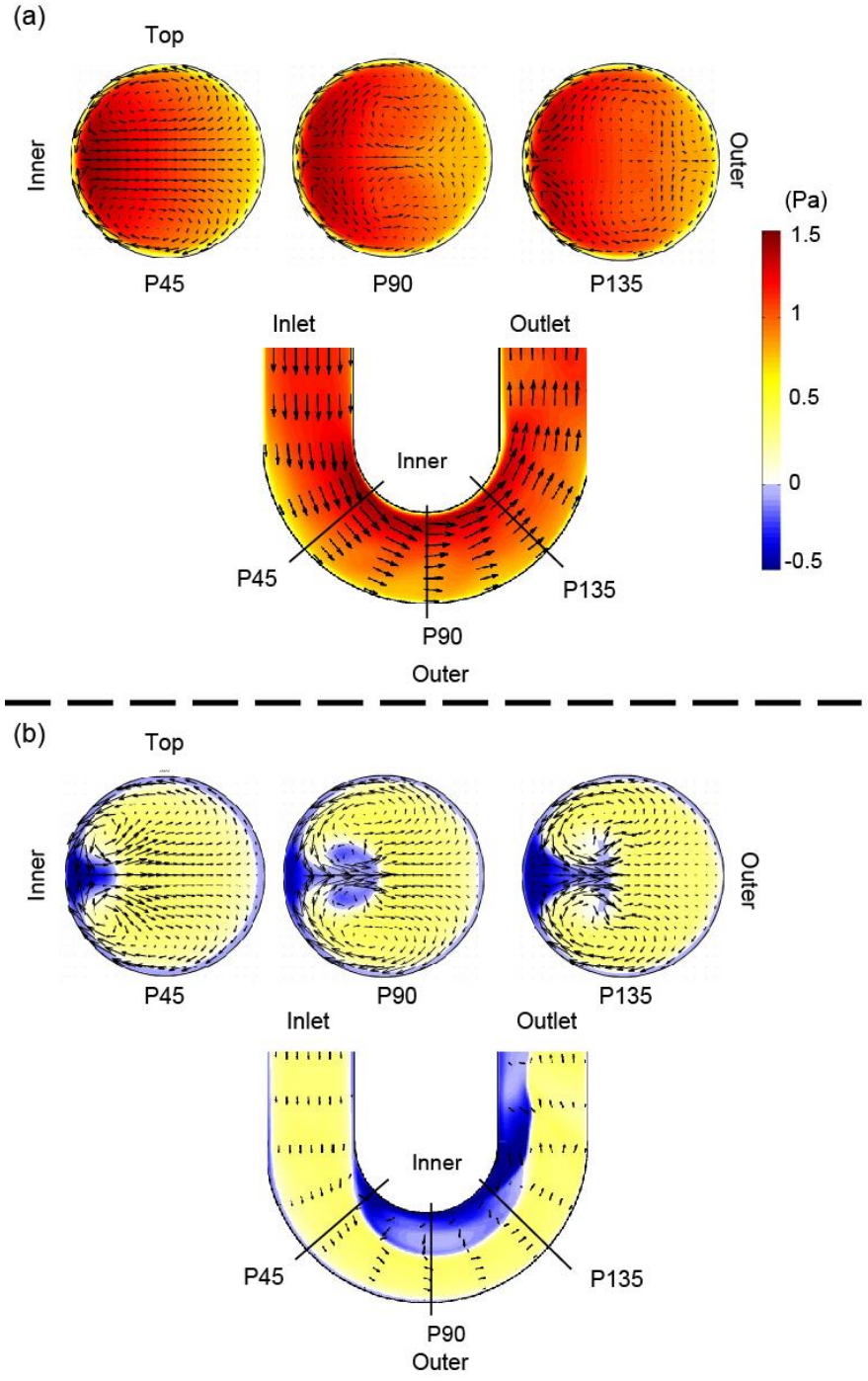
(a)
Top
Inner
Outer
P45
P90
P135
(Pa)
1.5
1
0.5
0
-0.5
Inlet
Outlet
Inner
P45
P135
P90
Outer
(b)
Top
Inner
Outer
P45
P90
P135
Inlet
Outlet
Inner
P45
P135
P90
Outer

Figure 4

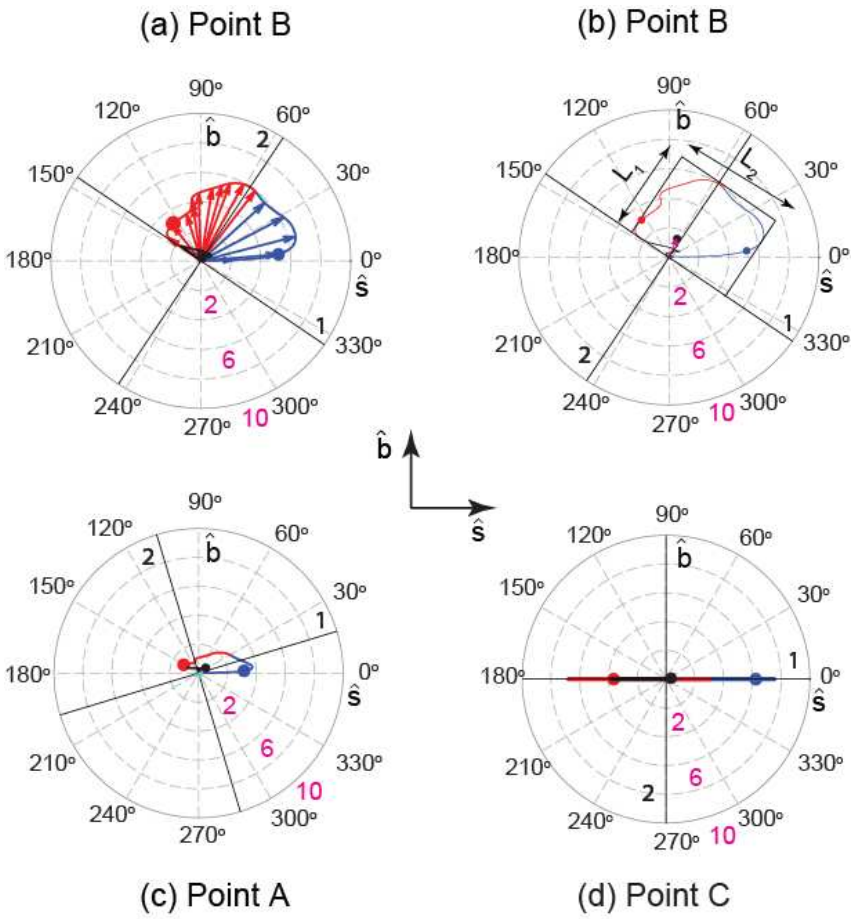

	$\lvert WSS_{mean} \rvert$ (Pa)	TAWSS (Pa)	transWSS (Pa)	OSI	AR
Point A	0.54	0.76	0.4	0.15	0.4
Point B	1.36	1.71	0.83	0.09	0.81
Point C	0.06	1.34	0.0	0.48	0.0`

Figure 5

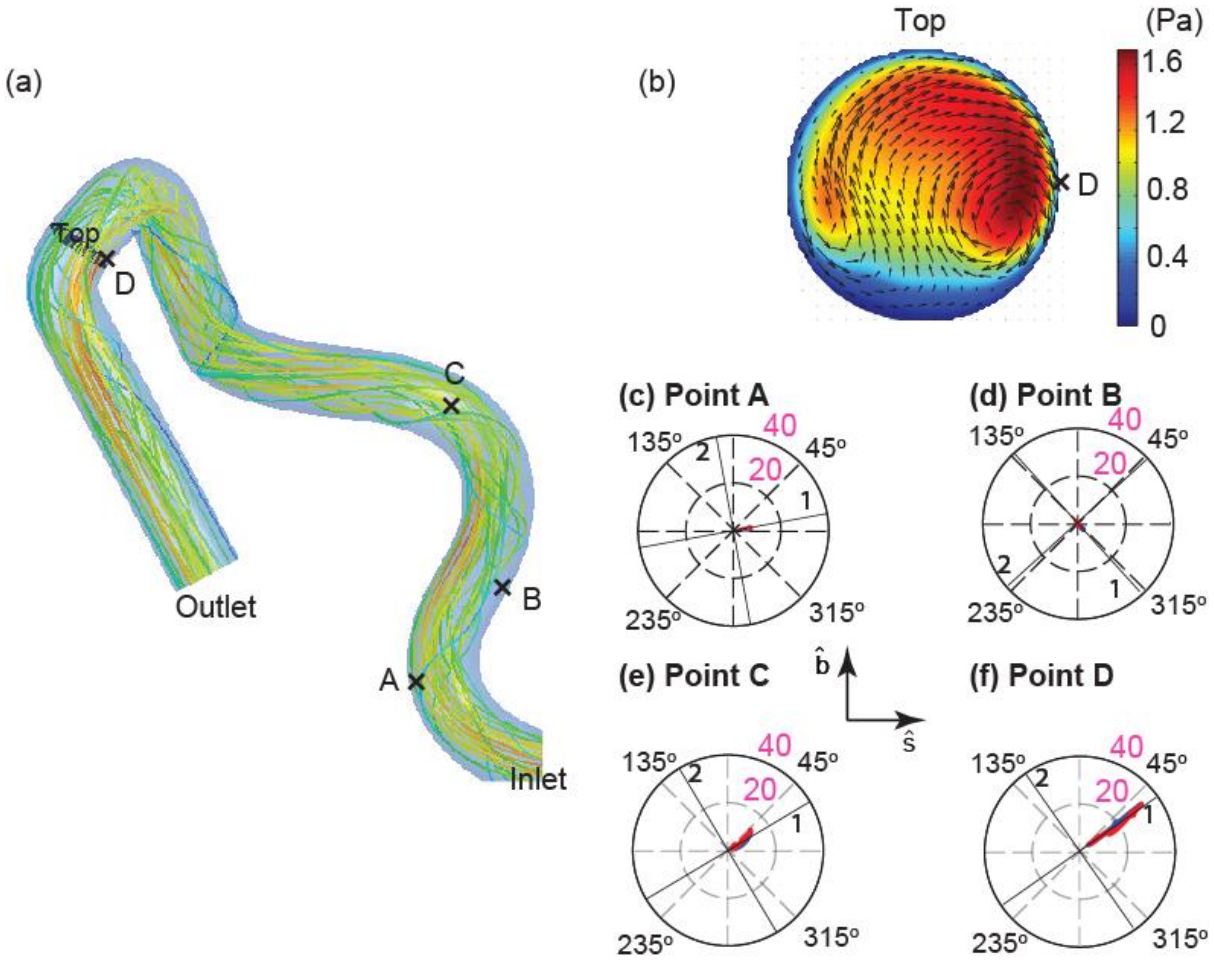
(a)
Top
D
C
B
A
Outlet
Inlet
(b)
Top
(Pa)
1.6
1.2
0.8
0.4
0
D
(c) Point A
(d) Point B
(e) Point C
(f) Point D
135°
45°
235°
315°
40
20
2
1
b̂
ŝ

Figure 6

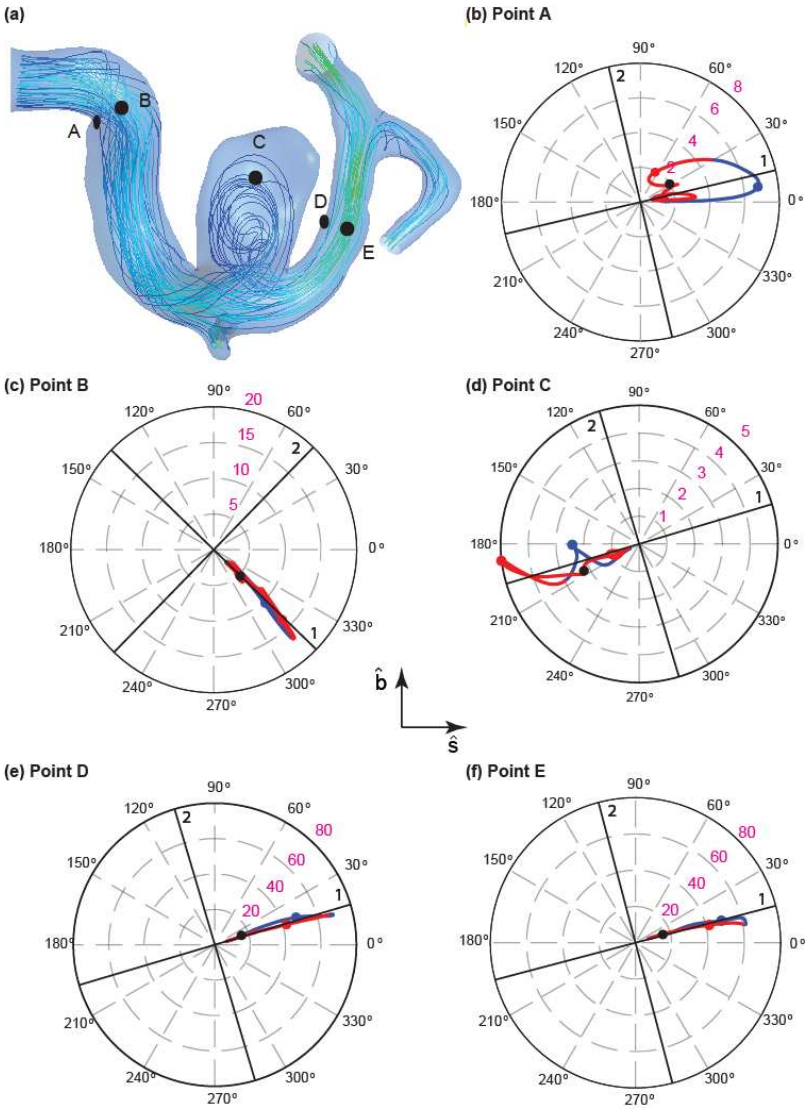

Figure 7

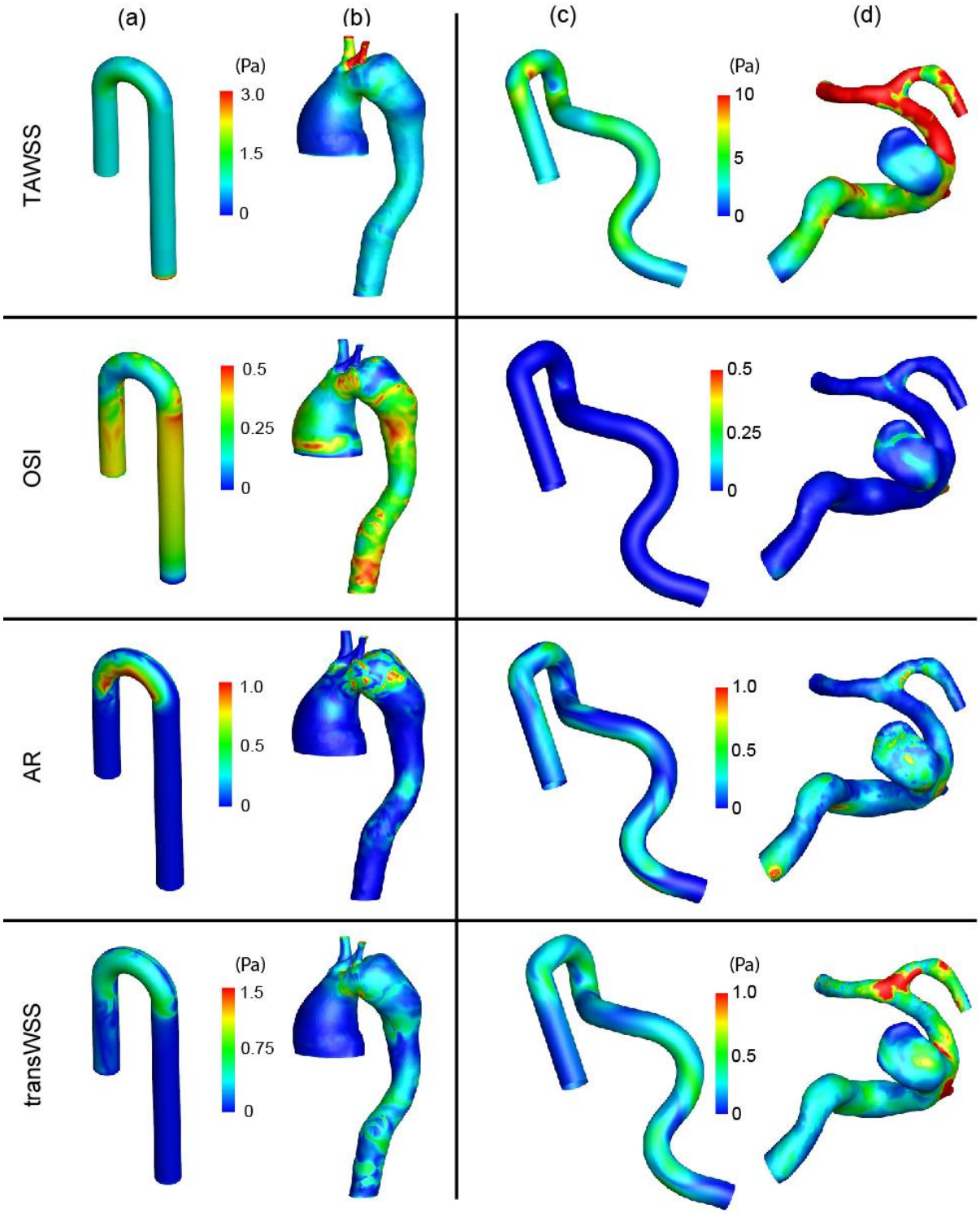

Table I:

	Equation	Description	Reference
Time Averaged Wall Shear Stress (TAWSS)	$TAWSS = \frac{1}{T}\int_{nT}^{nT+T} \lvert\vec{\tau}\rvert dt$	Time average of the WSS magnitude over a cardiac cycle	(He and Ku, 1996)
Mean shear stress ($\vec{\tau}_{mean}$)	$\vec{\tau}_{mean} = \frac{1}{T}\int_{nT}^{nT+T} \vec{\tau} dt$	Time average of the WSS vector over a cardiac cycle	(Arzani and Shadden, 2016)
Oscillatory shear index (OSI)	$OSI = \frac{1}{2}\left\{1 - \frac{\lvert\vec{\tau}_{mean}\rvert}{TAWSS}\right\}$	Oscillatory variation in the WSS	(Ku *et al*, 1985)
TransWSS	$transWSS = \frac{1}{T}\int_{nT}^{nT+T} \left\lvert \vec{\tau} \cdot \left(\vec{n} \times \frac{\vec{\tau}_{mean}}{\lvert\vec{\tau}_{mean}\rvert} \right) \right\rvert dt$	Time averaged magnitude of WSS components normal to the mean shear stress vector and the local surface normal ($\vec{n}$)	(Peiffer *et al*, 2013)
Anisotropy ratio (AR)	$AR = \frac{(\tau_{2(max)} - \tau_{2(min)})}{(\tau_{1(max)} - \tau_{1(min)})}$	The minimum ratio of breadth to the length of a rectangular box bounding the shear rosette. 1 and 2 are principal directions of the shear rosette	Current study

Table II

	Location	OSI	TAWSS (Pa)	AR	transWSS (Pa)
Control ICA	**A**	0.00	2.43	0.11	0.11
	B	0.00	1.03	0.1	0.04
	C	0.00	4.11	0.26	0.25
	D	0.00	9.61	0.08	0.21
Aneurysm ICA	**A**	0.00	2.25	0.43	0.46
	B	0.00	5.29	0.13	0.16
	C	0.00	2.44	0.31	0.28
	D	0.00	15.48	0.08	0.38
	E	0.00	16.51	0.13	0.50